Cellular and Molecular Bioengineering, Vol. 4, No. 2, June 2011 *(© 2010)* pp. 205–219
DOI: 10.1007/s12195-010-0141-z

A Semi-Automatic Method for Image Analysis of Edge Dynamics in Living Cells

LAWRENCE HUANG[1,2] and BRIAN P. HELMKE[1,2]

[1]Department of Biomedical Engineering, University of Virginia, P.O. Box 800759, Charlottesville, VA 22908-0759, USA; and [2]Robert M. Berne Cardiovascular Research Center, University of Virginia, Charlottesville, VA 22908, USA

(Received 14 May 2010; accepted 2 September 2010; published online 22 September 2010)

Associate Editor Yingxiao Peter Wang and Peter Butler oversaw the review of this article.

Abstract—Spatial asymmetry of actin edge ruffling contributes to the process of cell polarization and directional migration, but mechanisms by which external cues control actin polymerization near cell edges remain unclear. We designed a quantitative image analysis strategy to measure the spatiotemporal distribution of actin edge ruffling. Time-lapse images of endothelial cells (ECs) expressing mRFP-actin were segmented using an active contour method. In intensity line profiles oriented normal to the cell edge, peak detection identified the angular distribution of polymerized actin within 1 μm of the cell edge, which was localized to lamellipodia and edge ruffles. Edge features associated with filopodia and peripheral stress fibers were removed. Circular statistical analysis enabled detection of cell polarity, indicated by a unimodal distribution of edge ruffles. To demonstrate the approach, we detected a rapid, nondirectional increase in edge ruffling in serum-stimulated ECs and a change in constitutive ruffling orientation in quiescent, nonpolarized ECs. Error analysis using simulated test images demonstrate robustness of the method to variations in image noise levels, edge ruffle arc length, and edge intensity gradient. These quantitative measurements of edge ruffling dynamics enable investigation at the cellular length scale of the underlying molecular mechanisms regulating actin assembly and cell polarization.

Keywords—Actin ruffles, Planar cell polarity, Mechanotransduction, Endothelial cell.

INTRODUCTION

Directed cell migration plays an important role in many physiological and pathological processes, including angiogenesis, wound repair, and cancer metastasis. Persistently migrating cells must first acquire spatial asymmetry and directionality, an active process dependent on polarized remodeling of the cytoskeleton.[16] During the initial stages of cell polarization, cells actively probe the composition and rigidity of the extracellular matrix by extending actin-rich lamellipodia at cell edges in search for spatial cues. These structures contain a meshwork of polymerized actin filaments that may extend smoothly outward or perform wavelike motions known as edge ruffling.[2] Identifying the underlying mechanisms that guide directional edge ruffling and the establishment of cell polarity in response to external chemical and mechanical stimuli remains a critical challenge in developing strategies to engineer and control cell migration.

Precise characterization of edge ruffling dynamics remains difficult, since the degree and directions of edge ruffling are highly variable in both individual cells and across multiple cells. Histological labeling of F-actin by immunofluorescence or fluorescent phalloidin reveals higher intensity staining near cell edges with ruffles. In living cells expressing fluorescently-labeled actin, brightly labeled cell edges representing lamellipodia exhibit a characteristic convex shape with a concentrated band of polymerized actin at the rim. In phase-contrast time-lapse movies of living cells, lamellipodia appear as dark waves moving centripetally towards to the cell body. Investigators have relied on these distinct morphological features to manually identify sites of actin ruffling on the cell perimeter.[17,18,20,21] Visual scoring methods, however, are faced with several limitations. Manually defining the start and end locations of the ruffling edge is not only time consuming but also subject to investigator bias. Moreover, while broad lamellipodia may be consistently detected in polarized cells (e.g. cells migrating towards a chemoattractant), visual scoring becomes less accurate in cases where a preferred direction is not obvious and ruffles are shorter in length (e.g. quiescent

Address correspondence to Brian P. Helmke, Department of Biomedical Engineering, University of Virginia, P.O. Box 800759, Charlottesville, VA 22908-0759, USA. Electronic mail: helmke@virginia.edu

1865-5025/11/0600-0205/0 © 2010 Biomedical Engineering Society

cells in a confluent monolayer). Results from manual methods therefore only offer an overall picture of edge extension activity; they do not provide quantitative measures at adequate spatial resolution required to reflect signaling mechanisms associated with cell polarization.

To date, few quantitative measurements of edge feature dynamics at the cellular length scale have been performed. Recent image segmentation algorithms return accurate edge contours, allowing computation of membrane normal velocity and edge protrusion and retraction rates[6,19] in addition to more traditional readouts such as cell centroid position, area, and shape. However, techniques that track only the morphological changes of cell boundaries offer limited insight into structural dynamics inside the detected perimeter. Kymographs provide quantitative 1-D estimates of edge ruffle stability or velocity measurements in living cells at high spatiotemporal resolution.[12,14] Fluorescence intensity can be correlated with displacement measurements to characterize protein dynamics in specific regions of interest.[22] Alternatively, intensity line profiles and contour analysis have been used to quantify the distribution of fluorescently-labeled proteins in cells. For example, line profiles normal to the leading edge of migrating cells reflected the relative abundance of proteins such as tropomyosin, Arp2/3, and ADF/cofilin, proteins that regulate actin assembly in the region.[5,11] Intracellular distributions of actin and myosin as a function of radial distance from the cell edge have been measured using average or maximal intensities within a series of contours.[3,8] However, since kymographs focus on particular regions of interest on the cell perimeter (e.g. a distinct leading edge), and since line profiles or intensity values are averaged over large portions or the cell contour, these techniques do not reveal the 2-D spatial distribution of edge ruffling events that are relevant to elucidating mechanisms of directional sensing and adaptation.

In this study, we implemented a technique to quantitatively measure edge ruffling dynamics and actin-mediated planar cell polarity in living cells. Time-lapse images of individual cells expressing fluorescently-labeled actin were segmented using an active contour (snake) algorithm implemented in *ImageJ*.[1] Intensity line profiles oriented normal to the cell edge were computed for each pixel on the cell perimeter. Peak detection along the line profiles identified the angular distribution of polymerized actin within 1 μm of the cell edge and localized to lamellipodia and edge ruffles. Increases in actin intensity associated with filopodia and peripheral stress fibers were rejected. Compared to manual methods, the image analysis technique provides rapid, more objective, and more consistent readouts at improved spatial resolution. We demonstrate methods and applicability using time-lapse images of quiescent and serum-stimulated vascular endothelial cells.

METHODS

Cell Culture and Image Acquisition

Bovine aortic endothelial cells were maintained in Dulbecco's Modified Eagle Medium (DMEM, Gibco, Gaithersburg, MD) supplemented with 10% heat-inactivated newborn calf serum (HyClone, Logan, UT), 2.92 mg/mL L-glutamine (Gibco), 50 IU/mL penicillin and 50 μg/mL streptomycin (Gibco) as previously described.[13] Cells were transiently transfected with plasmid DNA encoding monomeric red fluorescent protein conjugated to β-actin (mRFP-actin, a kind gift from E. Fuchs, HHMI) using a liposome-mediated method according to manufacturer's recommendations (Lipofectin, Invitrogen, Carlsbad, CA). Serum-starved cells were maintained in DMEM containing 0.5% serum for 12 h and then were stimulated with 10% serum in DMEM. Fluorescence images of individual cells were acquired through a 60×/1.4 NA objective lens at an emission wavelength of 617 nm (red) using a DeltaVision RT Restoration Microscope (Applied Precision, Issaquah, WA). Image stacks with 4–5 optical sections were acquired for registration in the z-axis and deconvolved in *softWoRx* software (Applied Precision) using a constrained iterative algorithm and an experimentally measured point spread function.[15] After 3-D registration using fiducial markers on the coverslip as previously described,[13] single z-sections near the coverslip with the cell edge in focus were exported in TIFF format. Background subtraction and temporal normalization of fluorescence intensity were performed prior to image analysis.

Measurement of Edge Ruffling Dynamics in Living Cells

The image analysis strategy was designed to detect and measure the spatial distribution of fluorescence intensity peaks near cell edges indicative of actin polymerization that were localized to lamellipodia and edge ruffles but not filipodia and peripheral stress fibers. An active contour (snake) algorithm implemented as a plugin to *ImageJ*[1] was used to detect cell edges. Intensity line profiles directed normal to the cell edge were computed for each edge coordinate on the snake-defined contour. The orientation of the normal vector was determined from a 6-neighbor window along the contour. To attenuate noise, line profiles were smoothed using a 12-neighbor Gaussian window. A peak detection routine identified the locations of

polymerized actin on individual line profiles interpolated to 0.1-pixel precision. The rules for peak detection were as follows: (1) Local maximum had half-maximum intensity greater than the two adjacent local minima. (2) Local maximum had intensity I_{thr} (in arbitrary units, A.U.) greater than the adjacent local minima. This intensity change threshold ensured that peak heights were sufficiently greater than fluctuations due to noise and autofluorescence. Here, I_{thr} was set equal to the standard deviation of background noise. (3) Two adjacent local maxima in close proximity (separated by 0.1 μm or 1 pixel) were considered a single peak for the purpose of detection if the difference between peak heights was less than I_{thr}. (4) If the snake-defined edge had intensity greater than or equal to the half maximum of the local maximum closest to the cell edge, then it was assumed that the snake had underestimated the edge position. In this case, the intensity profile was extrapolated, and the adjusted edge intensity was set to one-half of the original edge intensity. Intensity peaks were resolved if these four conditions were met. Edge coordinates with resolved intensity peaks located less than 1 μm from the edge were grouped into components based on pixel connectivity to generate a 2-D spatial map of actin edge features.[10] To reduce false positives in peak detection, these connected components, hereafter referred to as "ruffling segments", were spatially filtered based on contour length. Ruffling segments with one-pixel length (i.e. island pixels) were removed; adjacent ruffling segments were bridged if their combined length was greater or equal to 8 (2×4) pixels and their separation distance was within 4 pixels. Finally, resultant ruffling segments with lengths 4 pixels or less were removed. Since 4 pixels on the snake-defined contour corresponded to ~1° on the circular interval, these filtering operations attenuated noise while retaining a minimum resolvable ruffling segment arc length of 1°.

In addition to broad lamellipodia and edge ruffles, filopodia and peripheral stress fibers are two other dynamic structures commonly found near cell edges. Filopodia are spike-like actin-rich bundles that project outward from the cell edge. Intensity profiles normal to their narrow perimeters represented a source of false positive results in lamellipodium detection. A smoothness constraint was imposed to exclude these features from the analysis. The cell perimeter was resampled at every 3–5 pixels, and the 2-D point-line distance d was evaluated for each pixel on the truncated contour $\xi(i)$ as

$$d(i) = \frac{|(x_2 - x_1)(y_1 - y_0) - (x_1 - x_0)(y_2 - y_1)|}{\sqrt{(x_2 - x_1)^2 + (y_2 - y_1)^2}},$$

where $(x_1, y_1) = \xi(i)$, $(x_0, y_0) = \xi(i + 1)$, and $(x_2, y_2) = \xi(i + 2)$. If d exceeded a distance threshold, the current pixel (x_0, y_0) was labeled as part of a filopodium projection and removed from ξ. The operation continued until the entire filopodium perimeter was captured. To reduce mislabeling of narrow intensity valleys on the 2-D contour as protrusions, r_0 was required to be greater than either r_1 or r_2, where r_n represents the radial distance to the geometric center of the contour. Coordinates on the original contour were mapped to the closest coordinate on ξ based on sum of squared differences (SSD) minimization. Peak detection results from pixels associated with filopodia were removed from subsequent analysis.

Intensity profiles along peripheral actin stress fibers parallel to the cell edge were the second major source of false positive results in edge ruffle detection. Due to their varying length and curvature, removal of these structures required manual intervention. 2-D feature maps generated from peak detection were overlaid with corresponding fluorescence images, and connected segments localized to peripheral stress fibers were rejected. Since peripheral stress fibers appear as long and wide arcs of high fluorescence intensity, manual rejection of these structures is unlikely to create subjective errors.

Angular distributions of intensity peaks localized to edge ruffles but not filopodia and peripheral stress fibers were accumulated for statistical analysis. To enable analysis across multiple cells with varying perimeter lengths, cell edge coordinates were grouped based on the polar angle with respect to the centroid position. The angular bin size was set as 1°. Perimeter bins were scored positive for edge ruffles if ruffling activity was detected in ≥50% of its constituent pixels. Vectorial statistical analysis was performed on the resulting grouped angular data. Image analysis and computations were performed using *ImageJ* and *MATLAB* (Mathworks, Natick, MA).

Test Images

Simulated test images were generated (Figs. 1a and 1b) to evaluate the performance of the snake algorithm after initialization using different combinations of adjustable parameters. Test images consisted of circular objects with radial intensity $I(r)$ defined by the logistic function $I(r) = I_{int}/(1 + e^{-kr})$, where I_{int} represented the intensity at the circle interior, and k controlled the intensity gradient. Parameter values were chosen to encompass estimates from live-cell images. Fluorescence intensity at the circle interior was set at 40 and 120 A.U. to simulate the edge region of cells with varying brightness. The corresponding edge

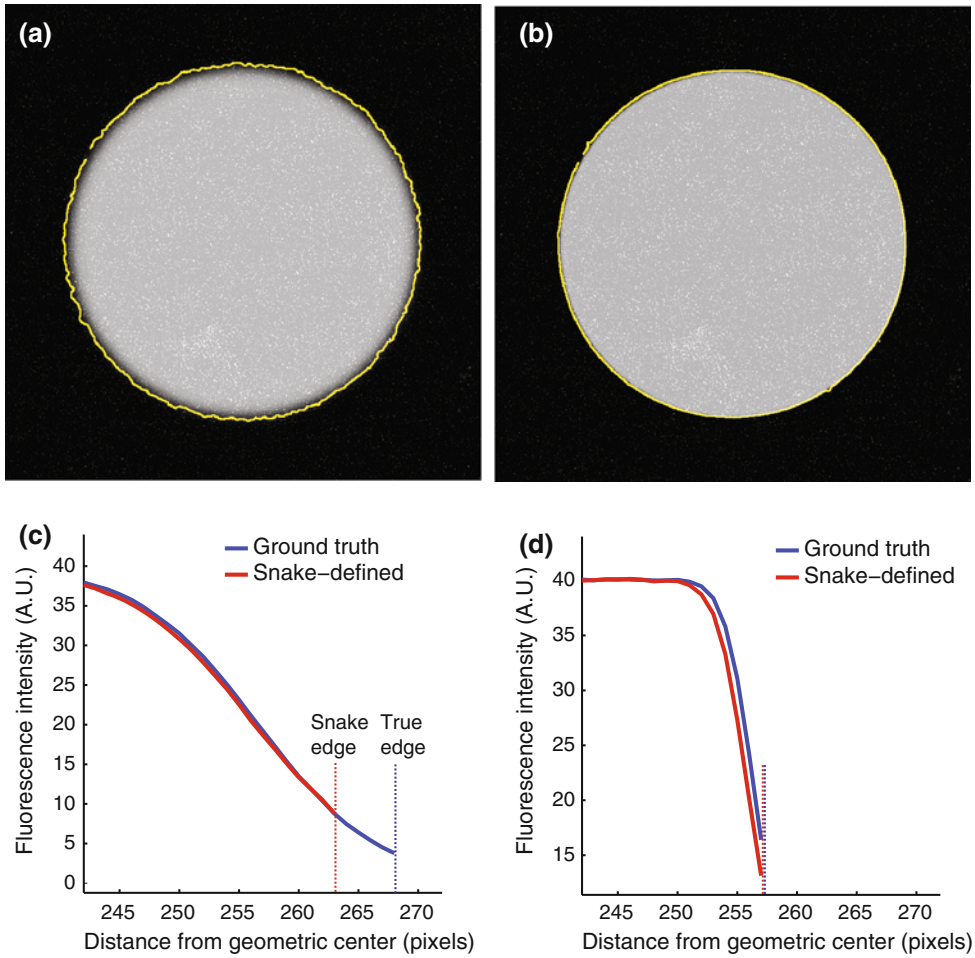

FIGURE 1. Comparison of edge boundary defined by the snake algorithm to the true edge. (a, b) Simulated test images with (a) small and (b) large intensity gradients at the edge of the circle. Representative snake contours are superimposed (yellow). (c, d) Circumferentially averaged intensity profiles from the snake-defined edge (red) and the true digitized circle edge (blue) for (c) small and (d) large edge intensity gradient images. Red and blue dotted lines indicate the snake-defined and true edge positions, respectively.

signal-to-noise ratios (SNR) were 1.2 and 4.0, respectively. SNR was computed as I/σ^2, where I = mean intensity, and σ^2 = noise variance computed over a 10-pixel wide edge region. The k parameter in the logistic function was set at 0.2 and 1.0 to simulate small and large intensity gradients at cell edges, respectively. In the case where the intensity gradient was small, a sharp, well-defined edge was absent, and visual methods for feature identification became less reliable. Experimentally acquired noise background images were superimposed. The same hand-drawn initialization contour was used for all test conditions.

A second series of test images were used to evaluate the performance of the semi-automatic method on known intensity distributions. Intensity at the circle interior I_{int} was set to 40, 60, 90, or 120 A.U. to yield approximate SNRs of 1.2, 2.0, 3.0, and 4.0, respectively. The k parameter in the logistic function was set at 1.0 or 0.2 to vary the edge gradient as previously described. To simulate polymerized actin at cell edges, intensity bands of varying segment arc lengths were superimposed within 1 μm of the snake-detected edge. These simulated edge features were 4 pixels wide in the radial direction and were centered on eight positions on the perimeter: 0°, 45°, 90°, 135°, 180°, 225°, 270°, and 315° (Fig. 3a). Band intensity values were estimated from cell images, and the corresponding normal line profiles possessed detectable features under the peak detection criteria (blue line *a* in Figs. 3b and 3c). It was assumed that the snake algorithm had successfully captured the cell edge. To reproduce a range of edge features ranging from small local bursts of actin polymerization to coordinated lamellipodium extensions, intensity band arc lengths were varied between 2°, 4°, 6°, 10°, and 24° on the circular interval, a range encompassing 0.5–6.7% of the total perimeter.

RESULTS

Segmentation by an Adaptive Snake Contour

Test images constructed of circular objects (Figs. 1a and 1b) were used to assess the accuracy of edge detection using a parametric snake algorithm. Initialization parameters including (1) the gradient threshold, (2) the α parameter that controlled the gradient image smoothness, and (3) the number of iterations were varied to determine combinations that enabled optimal edge detection in living cells with spatially heterogeneous edge intensity gradients. The regularization parameter that controlled internal smoothness of the snake contour was not investigated, since favorable levels of regularization in biological images cannot be determined using objects of generalized geometry as presented here. Instead, the analysis focused on parameters controlling the external forces that guide the snake to the object boundary. Noise in the fluorescence intensity image also appeared in the corresponding gradient image. While decreasing the Canny-Dériche operator α from its default value of 1.0 resulted in a smoother gradient image, the increased robustness to noise came at the expense of sharp edge features. When a moderate level of smoothing was applied using an α of 0.5, the resultant noise magnitude in the gradient image was estimated to be 2 ± 2 A.U. (mean $\pm$ standard deviation). In this study α was varied from 0.25 to 1 in order to test the snake on gradient images of varying smoothness. It was hypothesized that a corresponding gradient threshold between 10 and 25 A.U. was sufficient for edge detection.

The accuracy of the snake-defined line profile depended on the detected edge position and the direction of the normal vector used for intensity interpolation. We first assessed the ability of the snake to capture the true edge position. Test images were synthesized that simulated background-subtracted fluorescence images with low (Fig. 1a) and high (Fig. 1b) spatial intensity gradients at the test object edges. The true edge was defined to be the radial position with intensity greater than 1 A.U., as indicated on circumferentially averaged line intensity profiles (Figs. 1c and 1d, blue lines). The snake-defined edge contour and the true edge of the circle had the same sampling frequency and were aligned at their geometric centers before circumferentially averaging the radial intensity profiles. When the edge intensity gradient was small, corresponding to a blurred edge appearance (Fig. 1a), the snake algorithm consistently underestimated the true edge position (Fig. 1c, red line). When the edge intensity gradient was larger (Fig. 1b), the average radial edge coordinate detected by the snake algorithm (Fig. 1d, red line) was within 1 pixel of the true edge. In order to assess the accuracy of edge detection by the snake algorithm, the radial position of each edge coordinate on the snake-detected contour was compared to that of the nearest corresponding coordinate on the true edge. Results from individual pixels along the perimeter were compiled to compute the root mean squared error (RMSE) of edge position as a function of gradient threshold and Canny-Dériche α parameter values (Fig. 2a). When the edge intensity gradient was small, a small gradient threshold (10–15 A.U.) was required to obtain the most accurate edge position with a corresponding RMSE less than 5 pixels (Fig. 2a, left panels). The snake was more successful when a sharp edge was present, capturing the true edge with RMSE less than 1 pixel for most parameter combinations tested (Fig. 2a, right panels). RMSE values from images with different levels of maximum interior intensity (edge SNR) were not directly compared, since (1) the ground truth edge positions were different on the simulated fluorescence image and (2) the slope of the gradient image was different. In regions of small edge intensity gradient, the true edge at SNR = 4.0 had radius 4 pixels greater than the true edge at SNR = 1.2. The averaged snake-detected radius compared favorably; it was 3 pixels greater at SNR = 4.0 than at SNR = 1.2. In regions of large intensity gradient, the true edge position was identical (to the nearest pixel) at the two levels of SNR, and the average snake-detected edges fell within one pixel of each other. These results suggested that for the range of parameters tested, detection of edge position was relatively insensitive to noise.

Next, the accuracy of estimating the directions of normal vectors originating at the snake-defined edge was evaluated. Computation of the normal direction was performed using a 6-neighbor window on the edge map as described in "Methods" and was defined to be most accurate when the snake-detected contour was smooth. For each snake-detected edge coordinate, the normal vector direction was compared to that of the nearest corresponding coordinate on the true edge, and the average orientation error was computed along the perimeter as a function of gradient threshold and Canny-Dériche α parameter values (Fig. 2b). When the edge intensity gradient was small and edge SNR was low (Fig. 2b, upper left panel), the snake contour was less smooth with circularity ($=4\pi \times area/perimeter^2$) less than 0.9 and average orientation error of approximately 10°. Orientation error was minimized by selecting a large gradient threshold (20–25 A.U.). These results suggested that while a small gradient threshold may provide the most accurate average edge position, intensity line profiles originating from these positions did not represent vectors normal to the true

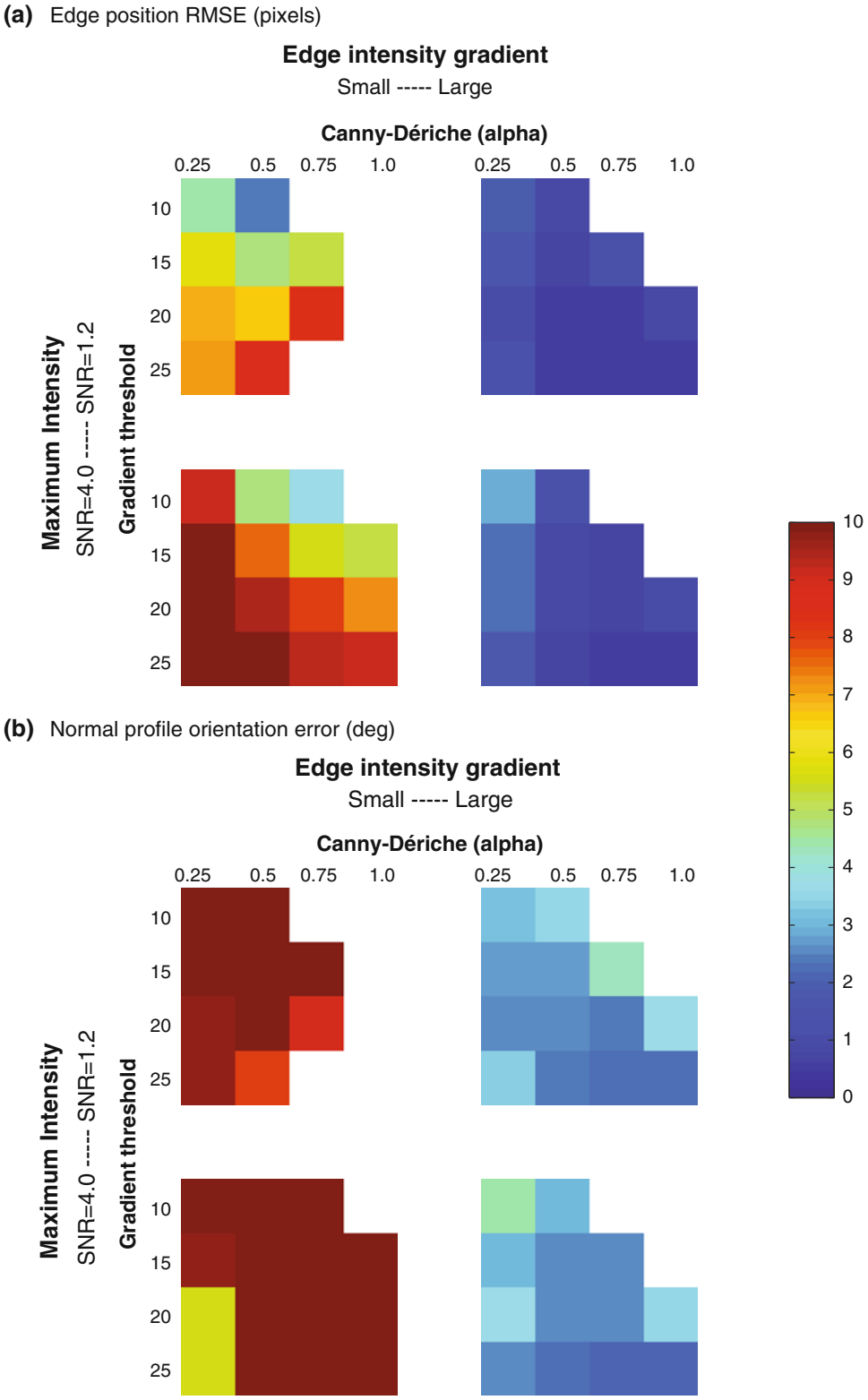

FIGURE 2. (a) Edge position and (b) normal orientation errors (color scale) as a function of snake parameters gradient threshold and Canny-Dériche operator α when comparing the snake-detected edge with the true edge.

edge. Similarly, in images with high edge SNR (steeper line profiles on the gradient image), accurate normal vectors with average orientation error less than 6° were achieved using a large gradient threshold and a high level of smoothing ($\alpha = 0.25$) (Fig. 2b, lower left panel). However, the detected edge positions were

more than 12 pixels away from the true edge. Accurate detection of edge features in regions of small intensity gradient therefore required a compromise between parameters that optimized edge position and normal vector orientation. In contrast, the snake contour was smooth in regions of large intensity gradient with circularity greater than 0.95 and average orientation error less than 3° (Fig. 2b, right panels). Low errors in both edge position and normal vector orientation in regions of large intensity gradient suggested that parameter optimization for line profile extraction should focus on the small intensity gradient case. In this case, a low level of smoothing (α = 0.5–0.75) and a small gradient threshold (10–15 A.U.) produced the most accurate average edge positions, whereas a high level of smoothing (α = 0.25) and a large gradient threshold (>20 A.U.) produced the most accurate normal vector orientations. Under most test conditions, increasing the number of iterations of the snake algorithm from 100 to 200 improved smoothness but resulted in further underestimation of the cell radius regardless of whether a sharp edge was present. Finally, the effect of noise on normal vector orientation was determined using images with different levels of edge SNR. The average orientation errors for edge SNRs of 1.2 and 4.0 were within 0.1° in both regions of small and large intensity gradient, further demonstrating that edge detection using the snake algorithm was insensitive to typical levels of image noise.

Effect of Image Parameters on Edge Feature Detection

The performance of the image analysis method in detecting edge ruffles was evaluated using test images. Edge features were generated in the region within 0–1 μm of the edges of circular test objects at known angular intervals (Figs. 3a–3c) as described in "Methods". For example, an intensity line profile perpendicular to the test object edge shows a large peak at the location of an edge feature (blue line *a*, Figs. 3b and 3c), but an intensity profile not located near a feature is smoothly increasing (red line *b*). Image segmentation was performed using initialization parameters that returned the most optimal trade-off between accurate average edge position and average normal vector orientation under all test conditions. Specifically, two combinations were tested with the snake algorithm set at 100 iterations: (1) a gradient threshold of 15 A.U. coupled with α of 0.5 and (2) a gradient threshold of 20 A.U. coupled with α of 0.25. In regions of small intensity gradient, the first set of parameters produced a more accurate average edge position (RMSE of 3.5 vs. 5.7 pixels), whereas the second set of parameters produced a smoother contour (orientation error of 7.9° vs. 5.4°). Angular distributions of intensity peaks were determined using the semi-automatic method and compared to ground truth. Successful detection was defined to occur when the algorithm correctly identified the positions of "positive" angular bins where intensity bands were superimposed. False positives were defined to be when angular bins with no superimposed intensity bands were detected. Detection rate was computed at eight positions on the circle perimeter as (number of successfully detected bins—number of false positive bins)/total number of positive bins. A mean detection rate above 90% averaged over the perimeter was considered accurate.

Figures 3d and 3e shows feature detection rates using the two sets of snake parameters at different levels of SNR, segment arc lengths, and edge intensity gradient. Edge features with arc length 6° or above were consistently detected for all levels of SNR and edge intensity gradient. Above this length, the mean detection rate averaged for all test conditions was 97 ± 3% (mean ± standard deviation). Due to a larger effect of pixel-to-pixel noise, the mean detection rate for segments with arc length below 6° decreased to 90 ± 11%, which was still considered accurate.

To test the effects of SNR, segment arc length, and edge intensity gradient on edge ruffle detection, results obtained using the two sets of snake parameters were pooled, and a 3-way ANOVA was performed. Mean detection rates at different levels of SNR were not statistically different (Fig. 4a), demonstrating that edge features of sufficient length were consistently detected even at the low level of SNR (SNR = 1.2) used to simulate a "worst case" scenario. However, the segment arc length and edge intensity gradient directly impacted mean detection rates. A *post hoc* multiple comparison test revealed a positive correlation between detection rate and segment arc length (Fig. 4b). For segments with arc length ≥4°, mean detection rate was significantly greater than for segments of 2° ($p < 0.05$, multiple comparison test). Comparing mean detection rates at different levels of edge intensity gradient (Fig. 4c) demonstrated that feature detection was more accurate in the absence of a sharp edge ($p < 0.05$, multiple comparison test). With the exception of 2° segments (89%), mean detection rates at all levels of image parameters tested were ≥90%, indicating successful detection. The ANOVA results suggested an interaction between segment arc length and edge intensity gradient. To explore this interaction, population marginal means were computed for each combination of the two variables, removing effects of SNR (Fig. 4d). For a combination of 2° segments and a large edge intensity gradient, the mean detection rate of 79% was significantly lower than that of the other groups, which had marginal means ≥90% ($p < 0.05$, multiple comparison test).

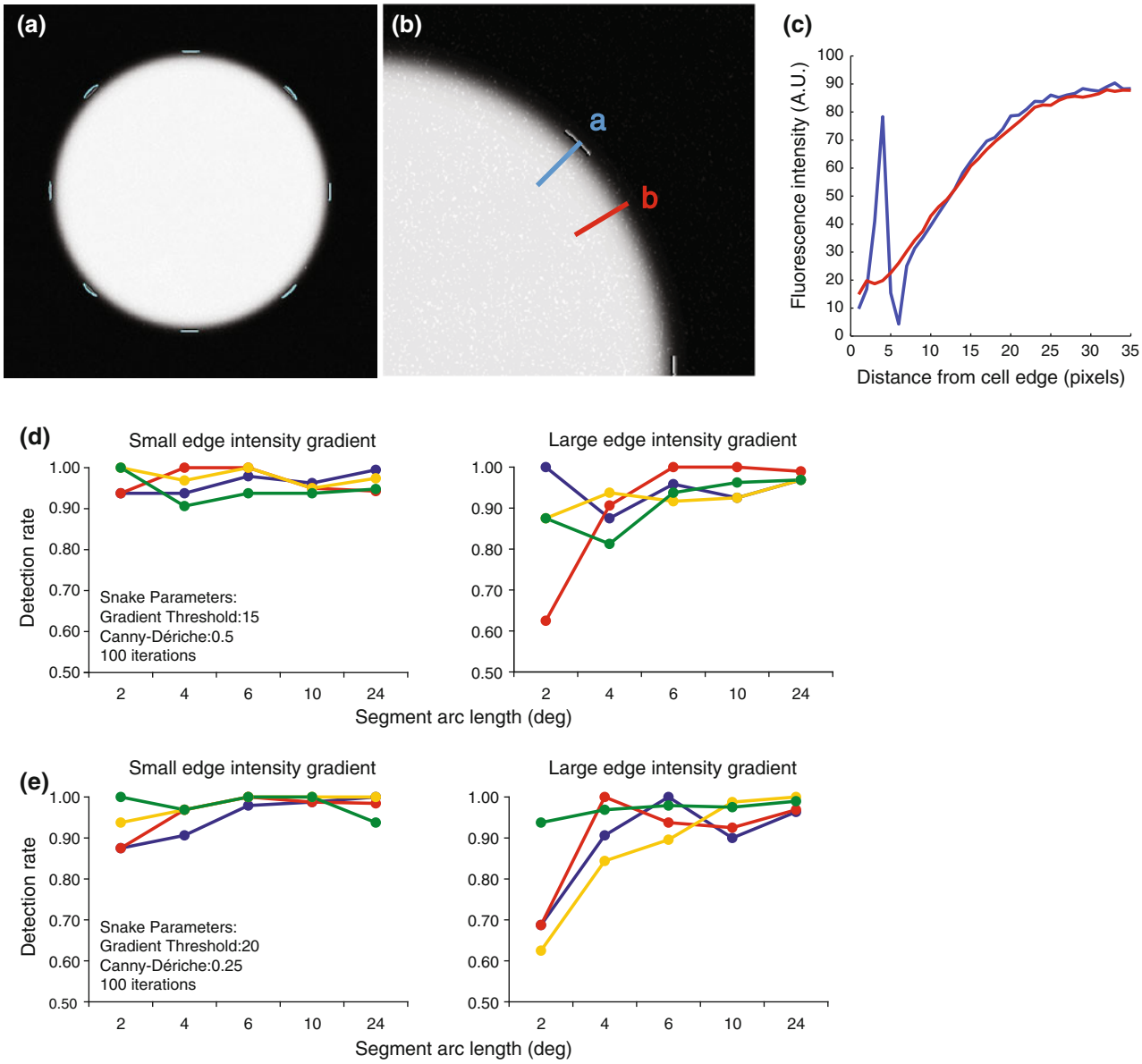

FIGURE 3. (a) Circular test object with simulated actin ruffles centered at 8 positions on the perimeter. Intensity bands were superimposed within 1 μm of the snake-detected edge. Cyan edge segments mark positions of detected intensity peaks. (b) Magnified view of an edge region of the test object with superimposed normal vectors at locations with (*a*; blue line) and without (*b*; red line) simulated actin ruffles. (c) Corresponding intensity line profiles at locations with (blue) and without (red) simulated detectable actin ruffles. (d–e) Edge feature detection rates using two sets of snake parameters at different levels of SNR, segment arc lengths, and edge intensity gradient. (d) Snake was initialized with a gradient threshold of 15 A.U. at an α parameter of 0.5 for 100 iterations. (E) Snake was initialized with a gradient threshold of 20 A.U. at an α parameter of 0.25 for 100 iterations.

Differences between other combinations of parameters were not significant.

Overall, edge features in test images were successfully detected using the image analysis techniques. For segment arc lengths above 2°, mean detection rates were ≥90% at all levels of SNR and edge intensity gradient. The data suggested that a minimum arc length of 4° was required for accurate feature detection under typical imaging conditions. Since an arc length of 4° (~16 pixels) corresponded to ~1% of the cell perimeter and represented small bursts of actin polymerization, the results indicated that larger lamellipodium extensions and changes in cell directionality would be easily detected.

Edge Ruffling Dynamics in Living Cells

The semi-automatic method was applied to measure edge ruffling dynamics in time-lapse images of living cells. Fluorescence images of subconfluent endothelial

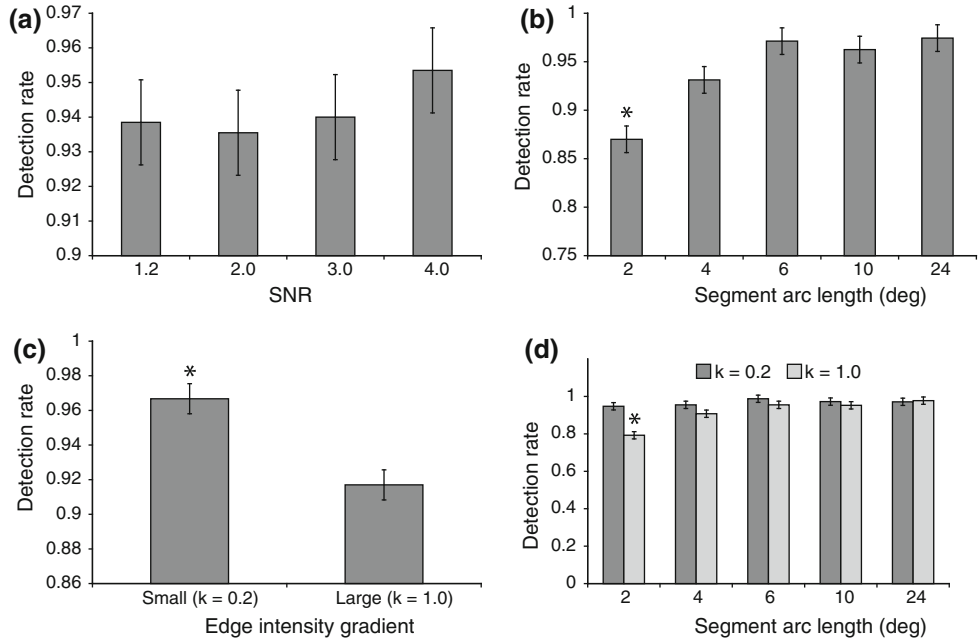

FIGURE 4. Effects of (a) SNR, (b) segment arc length, and (c) edge intensity gradient on ruffle detection. (d) Comparison of population marginal means for each combination of segment arc length and edge intensity gradient. Values shown are mean ± standard error. * Significant difference between groups ($p < 0.05$, multiple comparison test).

cells transiently expressing mRFP-actin were acquired. Edge coordinates were generated using the snake plugin initialized with a gradient threshold of 15 A.U. and α of 0.5 for 100 iterations. Figure 5 shows representative intensity profiles directed normal to the cell edge. Intensity peaks detected inside (0–1 μm) and outside (>1 μm) the edge region were labeled with red and green asterisks (*), respectively. The algorithm detected intensity peaks near the cell edge in profiles a and b (Figs. 5a and 5b), demonstrating insensitivity to absolute peak heights. In profiles c and d (Figs. 5c and 5d), cytoplasmic F-actin structure was detected, but edge intensity peaks were absent. A peripheral stress fiber appeared in profile e (Fig. 5e). Note that the same stress fiber with similar peak intensity as that measured in profile e was also detected approximately 5 μm away from the cell edge in profile f (Fig. 5f). Profile F also contained an edge ruffle, which was successfully detected. Contour smoothing automatically removed pixels with intensity profiles perpendicular to the tip of a protruding filopodium that were falsely detected as part of a ruffling edge (Fig. 6).

The following experiment demonstrates detection of changes in the degree of edge ruffling. Figure 7 shows time-lapse images of a serum-starved cell before (Fig. 7a) and after (Fig. 7b) stimulation with 10% serum. To quantify the degree of ruffling, the fraction of perimeter engaged in ruffling was computed as the ratio of the number of angular bins engaged in ruffling to the total number of angular bins. Addition of serum triggered a rapid burst of edge ruffling in cells, as indicated by the cyan perimeter contour segments. After 10 min, the fraction of the cell perimeter engaged in ruffling increased from 25% (90°/360°) to 76% (272°/360°).

Since the spatial asymmetry of actin polymerization was hypothesized to reflect the establishment of planar cell polarity, a nonparametric circular statistics approach[9] was used to assess spatial clustering of edge ruffling segments. Angular directions of edge ruffling segments were represented as unit vectors on the circular interval with vector angles θ_i ($i = 1,\ldots,N$) and were used to compute the mean resultant length $\overline{R}$ and the mean orientation angle $\bar{\theta}$. The Rayleigh test was used to determine whether the distribution of ruffling segment directions could be fitted with a unimodal circular distribution (null hypothesis: uniform distribution on the circle). Figure 8 shows time-lapse images of an endothelial cell in a subconfluent monolayer undergoing constitutive edge ruffling. Initially (t = 0:00), prominent membrane extensions were visually identified with orientations between 150 and 240° (Fig. 8, arrows). Statistical analysis on the angular distribution of edge ruffles revealed a mean resultant vector length that was significantly different from 0 ($p < 0.05$, Rayleigh test) and a mean ruffling direction of 194°. After 10 min (0:10), edge ruffles observed at t = 0:00 remained. In addition, new extensions developed with orientations between 0 and 30° (Fig. 8, arrows). Although over 55% of the ruffling bins

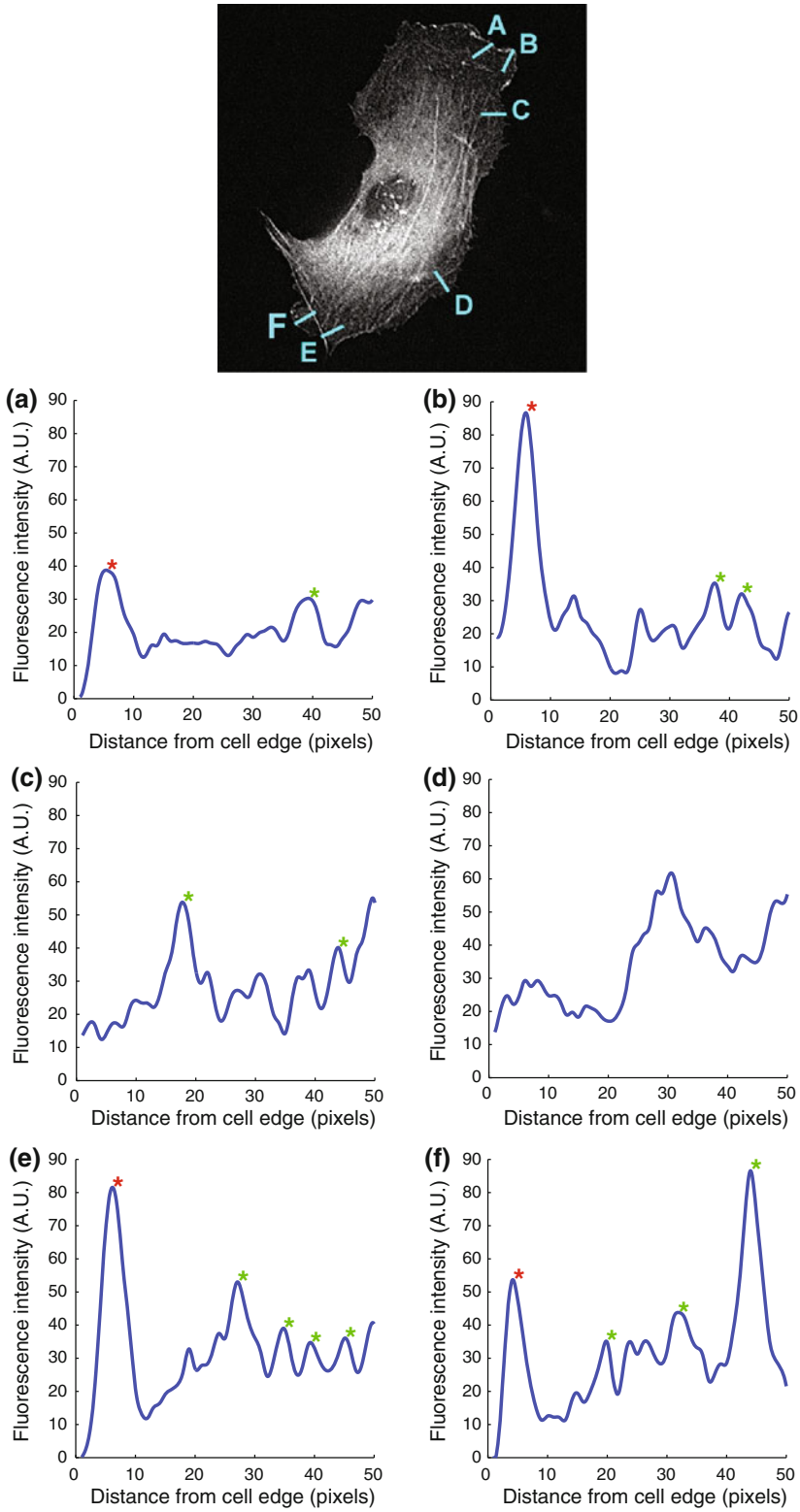

FIGURE 5. Endothelial cell expressing mRFP-actin distributed to internal stress fibers and edge ruffles. (a–f) Representative intensity line profiles normal to the cell edge. See text for explanation. Fluorescence intensity peaks detected inside a 1-μm-wide edge region (red asterisks) were assigned to ruffles. Peaks outside this edge region (green asterisks) were associated with cytoplasmic F-actin.

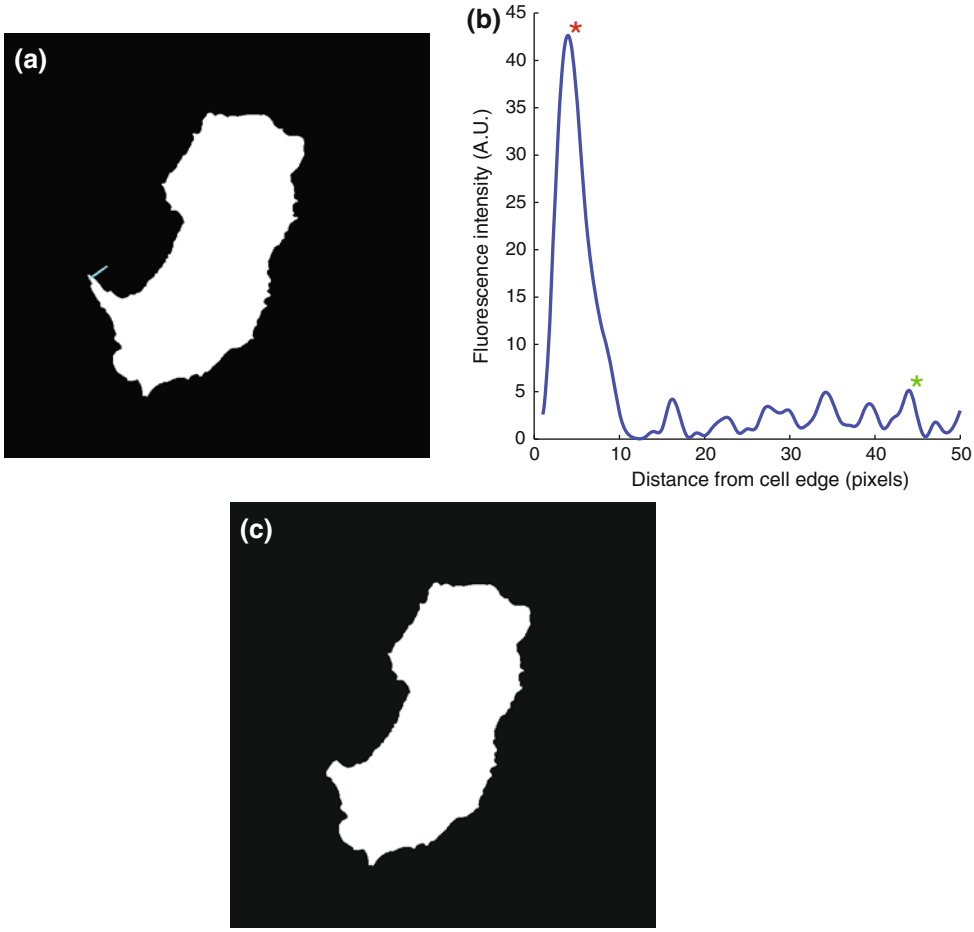

FIGURE 6. (a) Binary representation of a cell shape including filopodia. (b) Intensity profile perpendicular to a filopodium edge as indicated by the cyan line in (a). Polymerized actin in the filopodium was detected as a fluorescence peak (red asterisk). Pixel shot noise in the background region was detected as false positive peaks (green asterisks). (c) Cell shape after contour smoothing.

remain localized to the left half of the circle, the mean resultant length was not significantly different from 0, and the null hypothesis that ruffling directions were uniformly distributed could not be rejected ($p > 0.05$, Rayleigh test). In this case, a mean ruffling direction could not be defined, and the spatial asymmetry exhibited at t = 0:00 was lost (compare Figs. 8a and 8b). At t = 0:30, edge extensions oriented near 210° retracted, and edge ruffles formed at 270°, 330°, and 30° (Fig. 8, arrows). A unimodal distribution reemerged with edge ruffles clustered around a new mean orientation of 325° ($p < 0.05$, Rayleigh test). These data demonstrate accurate measurement of changes in edge ruffling directions and actin-mediated planar cell polarity.

DISCUSSION

This study demonstrates a semi-automatic image analysis method to detect changes in the spatiotemporal distribution of edge dynamics in living cells. The method assessed the distribution of fluorescence intensity within 1 μm of the cell boundary using techniques that minimized user error in scoring ruffle locations. Intensity peaks that corresponded with sites of actin polymerization and active ruffling were identified by peak detection.

Successful detection of edge features required a robust method for image segmentation. To determine the accuracy of line profile extraction using a parametric snake algorithm, the edge position and the normal vector orientation on the snake-detected contour were compared pixel-by-pixel with the true edge in test images. Since the region of interest consisted of a narrow 10-pixel wide window, minimizing errors in edge position was critical. In regions of large edge intensity gradient, the average snake-defined contour was accurate with RMSE < 1 pixel. Although larger errors of 3–5 pixels were observed in regions of small edge intensity gradient, the snake-defined edge coordinates had intensity values close to the

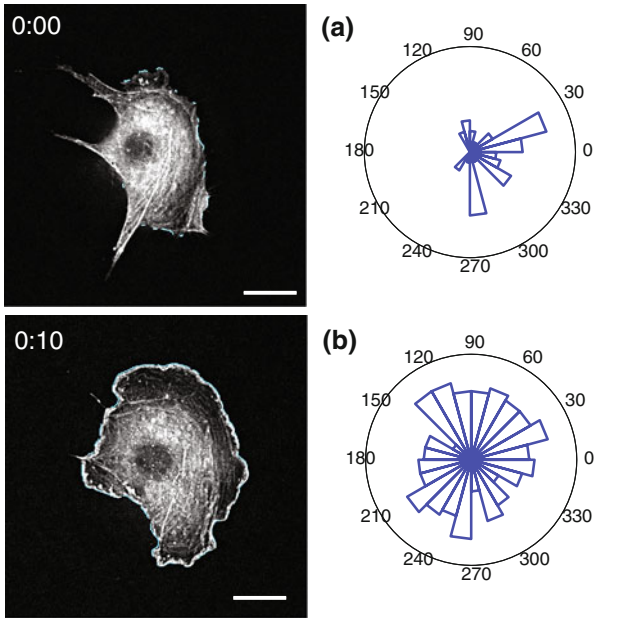

FIGURE 7. Snake contour-defined edge ruffles in a serum-starved endothelial cell expressing mRFP-actin. Initially (0:00), short segments of actin polymerization were detected (cyan edge segments). After 10 min of serum stimulation (0:10), the proportion of the cell perimeter engaged in ruffling increased from 25 to 76%. Scale bar, 10 μm. (a–b) Circular histograms of edge ruffle distribution before (a) and after (b) serum stimulation.

1-A.U. threshold that was used to define the true edge. Analysis of test images demonstrated that the loss of 3–5 pixels in these regions where the intensity profile was relatively flat did not affect edge feature detection. In fact, the mean detection rate was greater in the absence of a sharp edge. This observation was important because mRFP-actin intensity profiles rarely appeared as sharp edges in fluorescence images.

In addition to precise edge positions, accurate and consistent normal vector orientations were required to obtain the correct intensity line profiles for analysis. The value of the gradient threshold at a given level of smoothing determined the balance between contour edge position accuracy and contour smoothness. In regions of large edge intensity gradient, the smooth contour provided more accurate vector orientations that averaged within 3° of vectors normal to the true edge. When the edge intensity gradient was small, vector orientations were less accurate due to decreased smoothness of the snake contour, and the resultant average error was on the order of 10°. For the analysis of experimental data, we focused on optimizing detection in regions of low intensity gradient to find the highest level of edge position accuracy and contour smoothness. Although not tested here, the snake contour could be further fitted to the shapes of individual cells by adjusting the level of internal smoothness. Regularization may be important in regions of large intensity gradient, where small errors in edge position could result in the misdetection of edge features.

Detection of edge features was dependent on image parameters, including ruffling segment arc length and edge intensity gradient. The method was less reliable when the edge intensity gradient was large ($k = 1$ in the logistic function) and when the ruffling segments of interest were short in length (arc length of 2°). The mean detection rate was improved at longer ruffling segment lengths and/or a smoother cell edge (smaller k). Using test images, the minimum ruffling segment arc length required for accurate feature detection was 4° (~16 pixels). Above this threshold, the mean detection rate exceeded 90% at all levels of edge intensity gradient and SNR tested. Ruffling segment arc length was positively correlated with the segment pixel length. Detection of edge features of longer pixel lengths was enhanced in part due to reduced edge underestimation by the snake algorithm at these positions. Segments with fewer pixels were less favorable solutions for the snake in the presence of noise. Additionally, since a 12-neighbor filtering window was used to smooth intensity profiles with neighboring pixels prior to peak detection, intensity peaks in shorter ruffling segments were more likely to be lost. Detection accuracy was improved by filtering operations built into critical stages of the analysis routine. Noise in individual intensity line profiles were smoothed through spatial filtering with neighboring line profiles on the edge map prior to feature detection. 2-D ruffle maps were then filtered based on their perimeter pixel lengths. First, adjacent ruffles of sufficient lengths were bridged if their separation distance was small (≤1°). A 4-pixel (1°) length threshold was then imposed to prevent isolated pixels on the edge map from being misidentified as connected ruffles. Finally, in angular binning we required ≥50% of the constituent pixels in a bin to be engaged in ruffling. This operation served dual purposes: to further reject false positive results and to retain legitimate ruffling segments that spanned multiple bins. Collectively, these steps reduced susceptibility to noise both at the level of intensity profiles and in 2-D space.

How cells respond to biochemical and mechanical cues remains elusive. Analysis tools presented here build upon a parameterized cell contour to report more accurately and more rapidly edge structural dynamics and planar cell polarity compared with traditional investigator-based visual methods. The method is applicable for cell types that form lamellipodium extensions and edge ruffles and that can be transfected to express fluorescently tagged markers of actin edge features such as mRFP-actin. Ideally, at least 5 pixels are required for peak detection using the full-width half-maximum criterion. Since we defined the region of

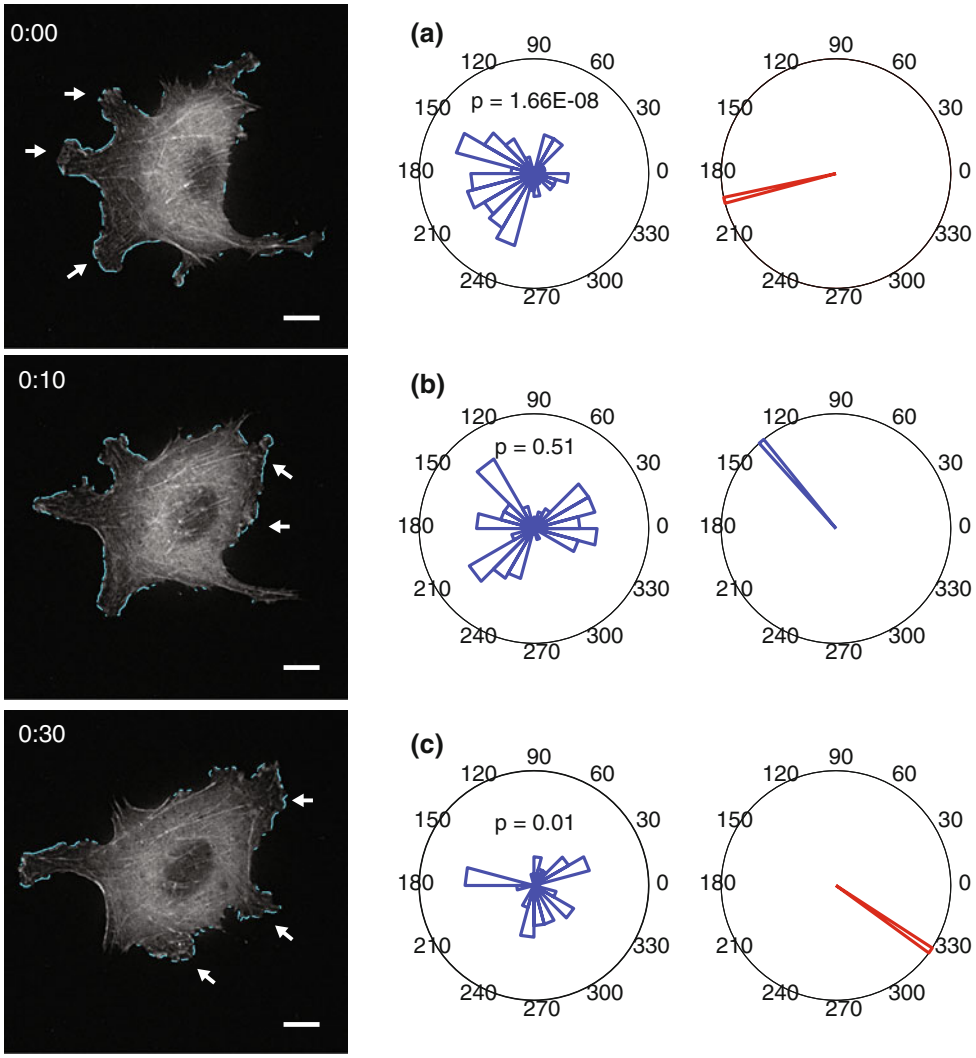

FIGURE 8. Snake contour-defined edge ruffles in a subconfluent endothelial cell undergoing constitutive edge ruffling. Arrows indicate locations of prominent edge extensions. See text for explanation. (a–c) Rose plots show the spatial distribution of ruffles (left panel) and the resultant mean ruffling orientation (right panel; red bars, $p < 0.05$, Rayleigh-test; blue bars, not significant).

interest to include ≤1 μm from the cell edge, the magnification required for analysis at an acceptable level of precision was ≥5 px/μm. In order to maintain this level of precision using lower image magnifications, the spatial region-of-interest size would need to be increased. In this study, deconvolution was important in improving image signal-to-noise ratio for peak detection on intensity line profiles. For the optical sections in Fig. 7, deconvolution improved the mean intensity computed in a 10-pixel wide edge region by a factor of 1.4 (84/60 A.U., Fig. 7, 0:00) to 1.7 (92/53 A.U., Fig. 7, 0:10). Analysis of raw images without any additional image processing steps returned ruffling perimeters of 6 and 31% for the two optical sections, compared to 25 and 76% using deconvolved images. Therefore, depending on the quality of the input images, methods for improving signal-to-noise such as deconvolution, CCD pixel binning, or filtering may be required to obtain accurate results.

One requirement of the method is that the cell interior intensity must drop below the half-maximum intensity to allow peak detection, which may limit applicability for early spreading cells. Another limitation may arise in cases where ruffling segments are immediately adjacent to stress fiber segments and are recognized as one connected segment. In the latter case, the end point of the stress fiber must be manually defined to separate the two features. Finally, it is desirable for the method to be effective in detecting ruffling activity in cells within a confluent monolayer. Since feature detection was accurate where the intensity gradient near the cell edge was small, detection of ruffling segments in cells in a confluent monolayer will be successful as long as the cell of interest does not

have transfected neighbors expressing fluorescent labels in the same wavelength that would otherwise affect image segmentation.

Techniques such as fluorescence speckle microscopy have been used to analyze cytoskeleton and adhesion protein turnover at high subcellular spatial resolution.[4] The approach presented here represents a complementary strategy at the cellular length scale that, when accumulated across multiple cells in a monolayer or thin tissue, will identify regions of interest for analysis at higher spatiotemporal resolution. Previous contour analysis techniques measuring fluorescence intensities have successfully characterized the spatial distribution (e.g. front vs. rear) of key proteins involved in the establishment of cell polarity.[3,7] However, since those techniques involve averaging or filtering in the radial direction, they require the fluorescently-labeled protein to be highly compartmentalized (e.g. localized to the edge or some known distance from the edge) and to have low cytoplasmic background intensity. Structural features or the spatial distribution of proteins in the radial direction within the averaging window cannot be readily resolved, making them less attractive for use in tracking cytoskeletal or other structural proteins. The semi-automatic detection of edge features provides high spatial resolution both along the contour and in the radial direction, allowing time-lapse tracking of structural features in 2-D. In cases where a preferred direction exists, the method provides quantitative measurements useful for investigating mechanisms regulating actin edge dynamics and how directional ruffling may guide migration. For example, measuring dispersion of actin ruffling orientations in a group of cells may provide new information on the strength of response in a scratch wound or chemotaxis assay and suggest molecular interventions. Since edge features are scored based on variations in individual intensity line profiles and not raw intensity values, the routine is more sensitive to subtle changes along the contour and therefore may be equally applicable for use on cells that do not exhibit distinct structural asymmetry or rapid, extensive orientation responses (e.g. endothelial monolayers). Since measuring actin edge dynamics provides a tool that is predictive of shape alignment for investigating molecular mechanisms, the method presented here complements existing image analysis tools that quantify membrane morphodynamics by tracking edge contours alone.

In summary, we describe a novel image analysis method to quantitatively measure the magnitude and direction distribution of actin edge ruffling. The method is capable of capturing a rapid increase in edge ruffling in endothelial cells stimulated with serum. In addition, a statistical analysis enables detection of cell polarity, indicated by ruffling and lamellipodium extension in a preferred direction. The results improve on existing measures of polarity, including membrane dynamics at the leading edge obtained from kymographs, actin stress fiber alignment, and motility readouts from bulk migration studies. The analysis is robust to noise, different segment arc lengths, and variations in edge intensity gradient, as demonstrated using biological images. Moreover, its application is automated with the exception of peripheral stress fiber removal, which requires minimal user intervention. The present work enables investigation of the molecular mechanisms that regulate actin assembly and cell polarization and will provide new insight into how directional edge ruffling may control cell alignment at longer time scales.

REFERENCES

[1]Boudier, T. Developing a deformation model for complex-shaped contours. *Innov. Tech. Biol. Med.* 18:1–14, 1997.
[2]Bray, D., and J. G. White. Cortical flow in animal cells. *Science* 239:883–888, 1988.
[3]Dalous, J., E. Burghardt, A. Muller-Taubenberger, F. Bruckert, G. Gerisch, and T. Bretschneider. Reversal of cell polarity and actin-myosin cytoskeleton reorganization under mechanical and chemical stimulation. *Biophys. J.* 94:1063–1074, 2008.
[4]Danuser, G., and C. M. Waterman-Storer. Quantitative fluorescent speckle microscopy of cytoskeleton dynamics. *Annu. Rev. Biophys. Biomol. Struct.* 35:361–387, 2006.
[5]Desmarais, V., I. Ichetovkin, J. Condeelis, and S. E. Hitchcock-Degregori. Spatial regulation of actin dynamics: a tropomyosin-free, actin-rich compartment at the leading edge. *J. Cell Sci.* 115:4649–4660, 2002.
[6]Dobereiner, H. G., B. J. Dubin-Thaler, J. M. Hofman, H. S. Xenias, T. N. Sims, G. Giannone, M. L. Dustin, C. H. Wiggins, and M. P. Sheetz. Lateral membrane waves constitute a universal dynamic pattern of motile cells. *Phys. Rev. Lett.* 97:038102, 2006.
[7]Dormann, D., T. Libotte, C. J. Weijer, and T. Bretschneider. Simultaneous quantification of cell motility and protein-membrane-association using active contours. *Cell Motil. Cytoskel.* 52:221–230, 2002.
[8]Ehringer, W. D., S. Yamany, K. Steier, A. Farag, F. J. Roisen, A. Dozier, and F. N. Miller. Quantitative image analysis of F-actin in endothelial cells. *Microcirculation* 6:291–303, 1999.
[9]Fisher, N. I. Statistical Analysis of Circular Data. Cambridge: Cambridge University Press, 1993.
[10]Gonzalez, R. C., and R. E. Woods. Digital Image Processing. Reading, MA: Addison-Wesley, 1992.
[11]Gupton, S. L., K. L. Anderson, T. P. Kole, R. S. Fischer, A. Ponti, S. E. Hitchcock-Degregori, G. Danuser, V. M. Fowler, D. Wirtz, D. Hanein, and C. M. Waterman-Storer. Cell migration without a lamellipodium: translation of actin dynamics into cell movement mediated by tropomyosin. *J. Cell Biol.* 168:619–631, 2005.
[12]Harms, B. D., G. M. Bassi, A. R. Horwitz, and D. A. Lauffenburger. Directional persistence of EGF-induced cell

migration is associated with stabilization of lamellipodial protrusions. *Biophys. J.* 88:1479–1488, 2005.
[13]Helmke, B. P., R. D. Goldman, and P. F. Davies. Rapid displacement of vimentin intermediate filaments in living endothelial cells exposed to flow. *Circ. Res.* 86:745–752, 2000.
[14]Hinz, B., W. Alt, C. Johnen, V. Herzog, and H. W. Kaiser. Quantifying lamella dynamics of cultured cells by SACED, a new computer-assisted motion analysis. *Exp. Cell Res.* 251:234–243, 1999.
[15]Hiraoka, Y., J. W. Sedat, D. A. Agard, and D. A. Agard. Determination of three-dimensional properties of a light microscope system: partial confocal behavior in epifluorescence microscopy. *Biophys. J.* 57:325–333, 1990.
[16]Horwitz, R., and D. Webb. Cell migration. *Curr. Biol.* 13:R756–R759, 2003.
[17]Katsumi, A., J. Milanini, W. B. Kiosses, M. A. Del Pozo, R. Kaunas, S. Chien, K. M. Hahn, and M. A. Schwartz. Effects of cell tension on the small GTPase Rac. *J. Cell Biol.* 158:153–164, 2002.
[18]Li, S., P. J. Butler, Y. Wang, Y. Hu, D. C. Han, S. Usami, J.-L. Guan, and S. Chien. The role of the dynamics of focal adhesion kinase in the mechanotaxis of endothelial cells. *Proc. Natl. Acad. Sci. U.S.A.* 99:3546, 2002.
[19]Machacek, M., and G. Danuser. Morphodynamic profiling of protrusion phenotypes. *Biophys. J.* 90:1439–1452, 2006.
[20]Masuda, M., and K. Fujiwara. The biased lamellipodium development and microtubule organizing center position in vascular endothelial cells migrating under the influence of fluid flow. *Biol. Cell* 77:237–245, 1993.
[21]Pankov, R., Y. Endo, S. Even-Ram, M. Araki, K. Clark, E. Cukierman, and K. M. Yamada. A Rac switch regulates random versus directionally persistent cell migration. *J. Cell Biol.* 170:793–802, 2005.
[22]Rottner, K., B. Behrendt, J. V. Small, and J. Wehland. VASP dynamics during lamellipodia protrusion. *Nat. Cell Biol.* 1:321–322, 1999.